

# Realization of Qi-Wu-Zhang model in spin-orbit-coupled ultracold fermions

Ming-Cheng Liang<sup>1,2†</sup>, Yu-Dong Wei<sup>1,2†</sup>, Long Zhang<sup>1,2†</sup>, Xu-Jie Wang<sup>1,2</sup>, Han Zhang<sup>1,2</sup>, Wen-Wei Wang<sup>1,2</sup>, Wei Qi<sup>1,2</sup>, Xiong-Jun Liu<sup>1,2,3\*</sup>, and Xibo Zhang<sup>1,2,4\*</sup>

<sup>1</sup>*International Center for Quantum Materials,*

*School of Physics, Peking University, Beijing 100871, China*

<sup>2</sup>*Collaborative Innovation Center of Quantum Matter, Beijing 100871, China*

<sup>3</sup>*Shenzhen Institute for Quantum Science and Engineering and Department of Physics,  
Southern University of Science and Technology, Shenzhen 518055, China and*

<sup>4</sup>*Beijing Academy of Quantum Information Sciences, Beijing 100193, China*

Based on the optical Raman lattice technique, we experimentally realize the Qi-Wu-Zhang model for quantum anomalous Hall phase in ultracold fermions with two-dimensional (2D) spin-orbit (SO) coupling. We develop a novel protocol of pump-probe quench measurement to probe, with minimal heating, the resonant spin flipping on particular quasi-momentum subspace called band-inversion surfaces. With this protocol we demonstrate a continuous crossover between 1D and 2D SO couplings by tuning the relative phase between two coherent Raman couplings, and detect the non-trivial topological band structures by varying the two-photon detuning. The non-trivial band topology is also observed by slowly loading the atoms into optical Raman lattices and measuring the spin textures. Our results show solid evidence for the realization of the minimal SO-coupled quantum anomalous Hall model, which can provide a feasible platform to investigate novel topological physics including the correlation effects with SO-coupled ultracold fermions.

---

\* Corresponding authors. Emails: xiongjunliu@pku.edu.cn and xibo@pku.edu.cn

Quantum anomalous Hall (QAH) effect denotes the quantum Hall effect without the Landau levels due to an external magnetic field [1, 2]. Over three decades ago, Haldane proposed the first model for the QAH effect in a honeycomb lattice [3], while the QAH phase has been realized and widely studied only in the recent years [4–6] in solid-state experiments based on the considerable progress of topological insulators [7, 8]. Currently, to realize the QAH effect at high temperature and in highly controllable systems with large band gaps is of particular interests [9].

There exist two distinct and early fundamental models for the QAH effect. One is the aforementioned Haldane model with staggered flux in two-dimensional (2D) honeycomb lattices for spinless fermions [3]. The other is the Qi-Wu-Zhang model for spin-1/2 fermions in square lattices, where the QAH effect is driven by 2D spin-orbit (SO) coupling [10, 11]. While these two minimum models have not been strictly implemented in solid-state materials, progress has been made in ultracold atoms. The Haldane model was experimentally realized for ultracold fermions in a periodically modulated optical honeycomb lattice [12]. At the same time, a novel scheme based on the optical Raman lattices was proposed to realize the Qi-Wu-Zhang model and 2D SO couplings for ultracold fermions [13, 14]. The follow-up studies have been achieved for Bose-Einstein condensates with 2D SO couplings [15–17]. Nevertheless, so far the Qi-Wu-Zhang model has not been realized in any fermionic quantum system. Implementing this model in ultracold Fermi gases will provide a versatile experimental platform to realize novel topological materials and further explore correlation physics in interacting topological systems.

Alkaline-earth atoms (AEAs) have potential advantages for realizing high-dimensional SO couplings and topological phases with ultracold fermions. In AEAs, a narrow-linewidth intercombination transition or a clock transition [18] has enabled the implementation of one-dimensional (1D) SO couplings [19, 20], where the heating effect due to spontaneous emission is significantly suppressed. Besides, AEAs enable an unique technique, the optical a.c. Stark shift [21], to achieve highly stable and spin-dependent ground-state energy shifts [19, 22] and realize SO-coupled systems with long lifetime.

In this work, we report the first experimental realization of the Qi-Wu-Zhang model in a fermionic system. We implement this model using strontium ( $^{87}\text{Sr}$ ) Fermi gases with 2D SO couplings induced by optical Raman lattices. A controlled crossover between 1D and 2D SO couplings and the band topology are observed with a new protocol of pump-probe quench measurement developed here, which employs a Raman pulse to drive momentum-dependent spin-flipping. The identification of band topology is further supported by measuring the spin texture in quasi-momentum space after slowly loading the fermions into optical Raman lattices. Our work lays an

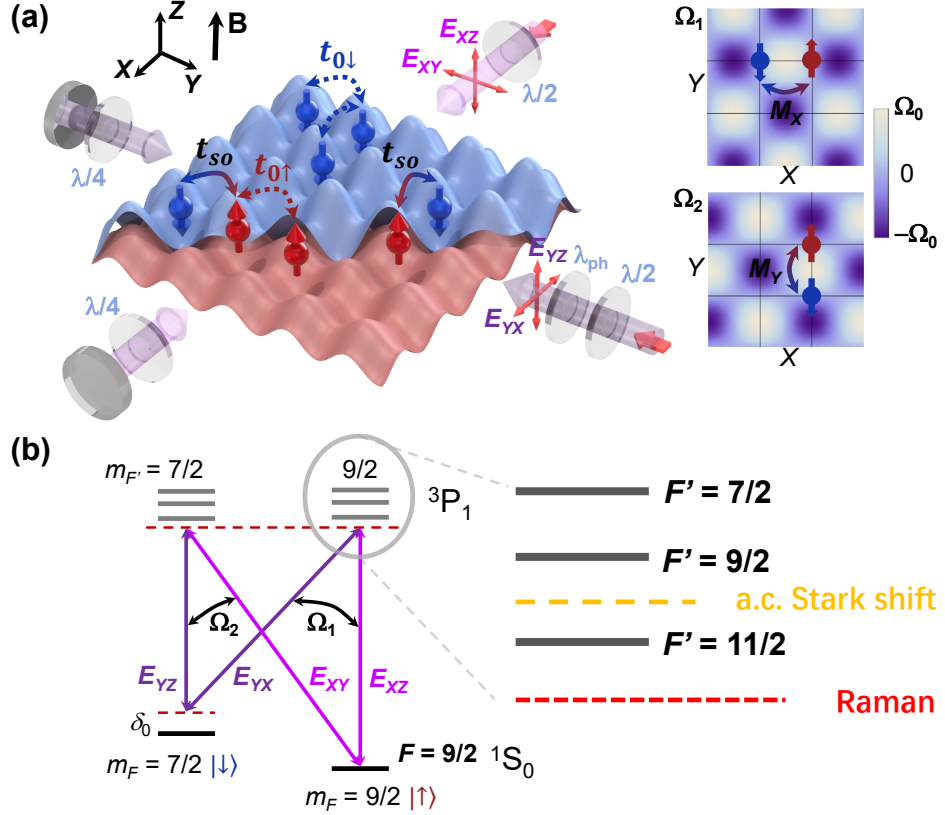


FIG. 1. Optical Raman lattice scheme for realizing the Qi-Wu-Zhang model and 2D SO couplings for ultracold fermions. (a) Experimental setup. The magnetic field  $\mathbf{B}$  along the  $Z$  direction defines the quantization axis of atoms. Two incident lasers are reflected to construct 2D optical lattices and Raman coupling lattices. The strengths of optical lattices are different for the two spin states (red for  $|↑\rangle$  and blue for  $|↓\rangle$ ). Two sets of Raman couplings ( $\Omega_1$  and  $\Omega_2$ ) are formed with their maximum values residing in between atomic positions (grid points). (b) Energy level diagram and the Raman coupling scheme. The relative phase  $\delta\varphi$  between  $\Omega_1$  and  $\Omega_2$  is controlled by a composite waveplate  $\lambda_{\text{ph}}$  shown in (a).

experimental foundation for further studies of topological physics with ultracold fermions.

*Experimental setup.*—We realize the Qi-Wu-Zhang model by implementing an optical Raman lattice scheme [14, 16] in  $^{87}\text{Sr}$  Fermi gases. As shown in Fig. 1(a), two linearly polarized laser beams propagate along the  $\hat{X}$  and  $-\hat{Y}$  horizontal directions, intersect at the atoms, and are each phase-shifted and retro-reflected to form 2D optical lattices for a pair of spin ground states:  $|↑\rangle \equiv |^1\text{S}_0 |F = \frac{9}{2}, m_F = \frac{9}{2}\rangle$  and  $|↓\rangle \equiv |^1\text{S}_0 |F = \frac{9}{2}, m_F = \frac{7}{2}\rangle$ . Two pairs of orthogonal polarization components,  $(E_{xz}, E_{yx})$  and  $(E_{yz}, E_{xy})$ , form two independent lattices of Raman couplings ( $\Omega_1$  and  $\Omega_2$ ) between the  $|↑\rangle$  and  $|↓\rangle$  states. This 2D optical Raman lattice configuration corresponds to a minimum

model of QAH Hamiltonian:

$$\hat{H} = \frac{\mathbf{p}^2}{2m} + V_{\text{latt}}(x, y) + \Omega_R(x, y) + \frac{\delta_0}{2} \sigma_z, \quad (1)$$

where  $m$  is the atomic mass,  $\sigma_{x,y,z}$  are Pauli matrices, and  $\delta_0$  is a two-photon Raman detuning. Here, the lattice potential matrix is given by

$$V_{\text{latt}}(x, y) = \begin{pmatrix} V_{\text{latt}\uparrow}(x, y) & 0 \\ 0 & V_{\text{latt}\downarrow}(x, y) \end{pmatrix}, \quad (2)$$

$$V_{\text{latt}\uparrow,\downarrow}(x, y) = V_{0X\uparrow,\downarrow} \cos^2 k_0 x + V_{0Y\uparrow,\downarrow} \cos^2 k_0 y,$$

and the Raman coupling matrix

$$\Omega_R(x, y) = \begin{pmatrix} 0 & \Omega_1 + e^{i\delta\varphi} \Omega_2 \\ \Omega_1^* + e^{-i\delta\varphi} \Omega_2^* & 0 \end{pmatrix} \quad (3)$$

shall generate the SO couplings, where  $\Omega_1(x, y) = \Omega_{01} \sin k_0 x \cos k_0 y$ ,  $\Omega_2(x, y) = \Omega_{02} \cos k_0 x \sin k_0 y$ ,  $k_0 = 2\pi/\lambda_0$  with  $\lambda_0 \approx 689.4$  nm, and  $\delta\varphi$  is the relative phase between two sets of Raman couplings. As illustrated in Fig. 1(b), these Raman beams are detuned relative to the  $^1\text{S}_0(F = \frac{9}{2}) \rightarrow ^3\text{P}_1(F' = \frac{11}{2})$  transition by -1 GHz. At this detuning, the optical lattice depths for  $|\uparrow\rangle$  and  $|\downarrow\rangle$  differ, and the two Raman coupling amplitudes have a ratio of  $\Omega_{01}/\Omega_{02} \approx 2.4 : 1$  under the same electric field intensities. We define a Zeeman term  $m_z$  as the sum of  $\delta_0/2$  and an offset determined by energy band structures, such that  $m_z$  equals 0 when the centers of the  $|\uparrow\rangle$  and  $|\downarrow\rangle$  bare ground energy bands align with each other.

To isolate the  $|\uparrow\rangle$  and  $|\downarrow\rangle$  states from the rest of the ten nuclear spin ground states and to control their energy difference, we apply an additional beam (called the shift beam) to induce optical a.c. Stark shifts for  $^{87}\text{Sr}$  atoms [23]. As shown in Fig. 1(b), the shift beam is blue-detuned by 690 MHz from the  $F = \frac{9}{2} \rightarrow F' = \frac{11}{2}$  transition, which separates out an effective spin-1/2 manifold with an energy difference of about 100 kHz between  $|\uparrow\rangle$  and  $|\downarrow\rangle$ . Based on fractional laser intensity noise controlled to the  $10^{-4}$  level, the stability of a.c. Stark shift is on the 10-Hz level, which is comparable to the ultrahigh stability in the Zeeman shift of an alkali metal atom under a 10-Gauss magnetic field with 1ppm control [24].

We prepare and detect SO-coupled fermions as follows. An almost spin-polarized ultracold  $^{87}\text{Sr}$  Fermi gas is prepared by optical pumping and subsequent evaporative cooling [23, 25]. About  $6 \times 10^4$  atoms are cooled to a temperature below 200 nK; 85% of these atoms are polarized into the  $|\uparrow\rangle$  state. The shift beam intensity is ramped to its final value, and the optical Raman lattices are then turned on suddenly (for quench measurements) or slowly (for slow loading) to generate

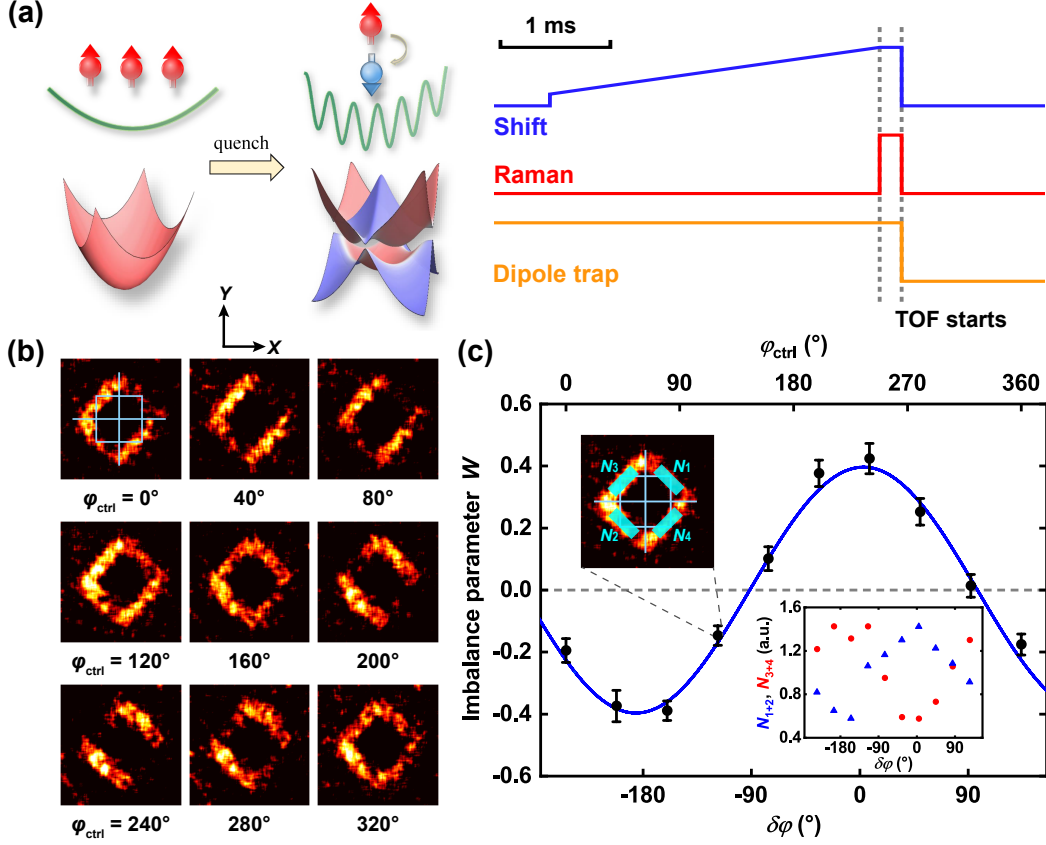


FIG. 2. Experimental realization of 2D SO coupling in ultracold fermions and 1D-2D crossover. (a) Diagram of the pump-probe quench measurement. (b) TOF images of atoms in the  $|\downarrow\rangle$  state under various relative phases between the two Raman couplings. The cyan square and cross mark the sizes of the first and second Brillouin zones, respectively. (c) The 1D-2D crossover of SO couplings, presented by the imbalance parameter  $W$  as a function of  $\varphi_{\text{ctrl}}$ . The black circles are measurements and the blue line is a fit. An optimum 2D SO coupling is achieved at  $W = 0$ , where the diffracted atomic population in the first and third quadrants ( $N_{1+2}$ ) equals that in the second and fourth quadrants ( $N_{3+4}$ ). Upper inset: illustration of  $N_{1,2,3,4}$ . Lower inset: original data of  $N_{1+2}$  and  $N_{3+4}$ . Error bars represent  $1\sigma$  statistical uncertainties.

SO couplings. In the end, we shut off all lasers within 1 microsecond and perform spin-resolved time-of-flight (TOF) measurements [19] to extract the atomic distributions  $n_{\uparrow,\downarrow}$  of the  $|\uparrow\rangle$  and  $|\downarrow\rangle$  states [23]. The spin texture is then given by the spin polarization  $P(\mathbf{q}) = \frac{n_{\uparrow}(\mathbf{q}) - n_{\downarrow}(\mathbf{q})}{n_{\uparrow}(\mathbf{q}) + n_{\downarrow}(\mathbf{q})}$  at each momentum  $\mathbf{q}$ .

*Pump-probe quench measurement.*—We develop a novel protocol of pump-probe quench measurement (PPQM) to probe SO couplings and energy band structures. As shown in Fig. 2(a), we initially prepare a cloud of atoms in the  $|\uparrow\rangle$  state without lattice, and suddenly shine a pulse of optical Raman lattice onto these atoms for a certain period of time. We then shut off all traps and

perform spin-resolved TOF measurement of atomic distributions, with the results being mapped to the quasi-momentum space of the optical Raman lattice. Due to the pulse, atoms in the  $|\uparrow\rangle$  state can be selectively pumped to  $|\downarrow\rangle$  at those quasi-momenta where the lowest spin-up and spin-down bands are inverted and coupled resonantly by two-photon Raman transitions, namely, at the band-inversion surface (BIS) which is a 1D ring or open line structure for the present system in 2D optical Raman lattices [26]. The BISs are an essential concept to characterize the non-trivial band topology with lower-dimensional information [26–34].

Compared with previous quench measurements [17, 32–41], the present PPQM has three distinct features. Firstly, optical lattices are not applied during the state preparation before the quench. Secondly, rather than varying the two-photon detuning (namely tuning  $m_z$ ) of the Raman coupling with a fixed strength in previous studies, we perform the quench by switching on the Raman coupling with a fixed detuning. Thirdly, instead of studying dynamical oscillations between two spin states, we only need a short pulse that generates the optical Raman lattice to pump atoms from initial state to the other state, with a pulse duration  $T_{\text{quench}} = 200 \mu\text{s}$  [23]. With these features, our PPQM protocol significantly simplifies the quench measurement and minimizes the application of the optical Raman lattice, which in turn maximally suppresses heating and other detrimental effects.

*SO coupling and band structure.*—We first demonstrate a continuous crossover between 1D and 2D SO couplings based on PPQM. As shown in Fig. 1(a), a variable composite waveplate  $\lambda_{\text{ph}}$  (with retardation  $\varphi_{\text{ctrl}}$ ) controls the relative phase  $\delta\varphi$  between two sets of Raman couplings [23]. Fig. 2(b) shows a series of momentum distribution of atoms transferred to  $|\downarrow\rangle$ , where the typical line segments along the  $\hat{X} + \hat{Y}$  and  $\hat{X} - \hat{Y}$  directions are consistent with the BIS under the corresponding experimental condition. Four groups of  $|\downarrow\rangle$  atoms (marked by  $N_1$  to  $N_4$  in the upper inset of Fig. 2(c)) appear in accordance with the four directions,  $(\pm k_0, \pm k_0)$ , of SO-coupling-induced momentum transfer. As  $\varphi_{\text{ctrl}}$  changes,  $N_{1+2}$  shows an out-of-phase variation with respect to  $N_{3+4}$  (lower inset of Fig. 2(c)). We further define the population imbalance

$$W = \frac{(N_1 + N_2) - (N_3 + N_4)}{(N_1 + N_2) + (N_3 + N_4)}, \quad (4)$$

and observe that  $W$  obeys a sinusoidal dependence on  $\varphi_{\text{ctrl}}$  with a period of  $360^\circ$  (Fig. 2(c)). The relative phase  $\delta\varphi$  is determined by a fit to the function  $W = W_{\text{max}} \cos(\delta\varphi)$  [16, 23]. Here,  $\delta\varphi = 0^\circ$  or  $-180^\circ$  corresponds to the case where only  $\sigma_x$  remains in the Raman coupling matrix, which is similar to 1D SO couplings for fermions in free space [19, 42, 43]. By contrast, the optimal 2D SO coupling is achieved at  $\delta\varphi = \pm 90^\circ$ , where balanced  $|\downarrow\rangle$  populations of  $N_1 \sim N_4$  are observed with

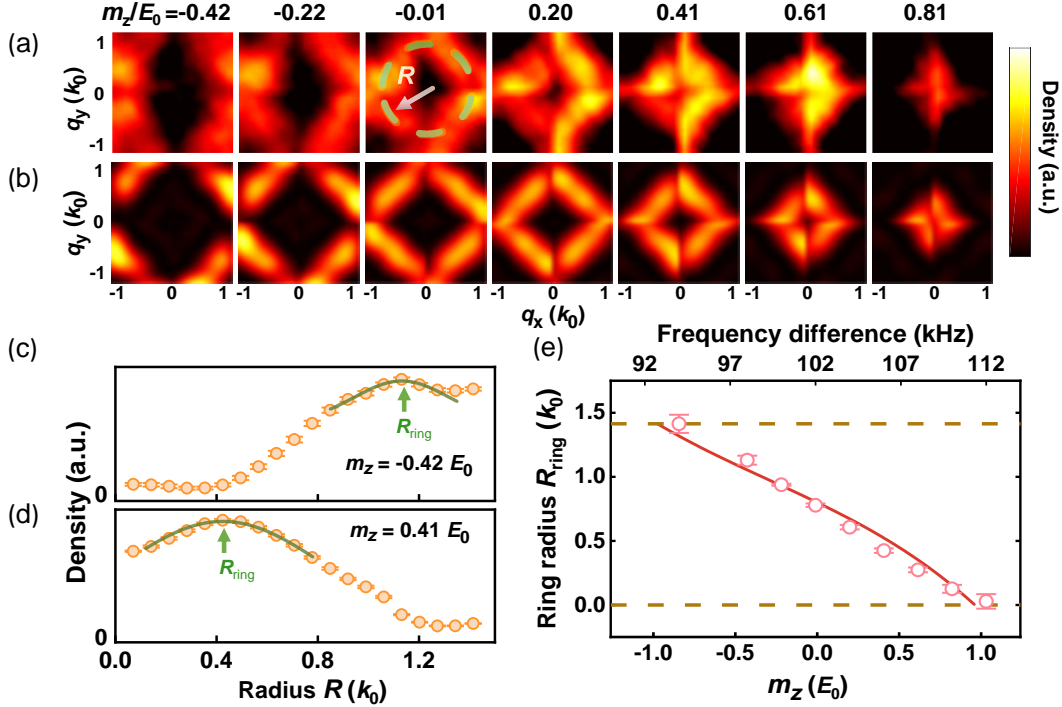


FIG. 3. Tomographic measurements of the energy band structures based on PPQM. (a) Experimental measurements of quasi-momentum distributions of atoms in  $|\downarrow\rangle$  after a quench. (b) Numerical simulations. (c) and (d) Azimuthally averaged profiles of characteristic 2D distributions in (a), under  $m_z/E_0 = -0.42$  and  $0.41$ , respectively. (e) Measured momenta ( $R_{\text{ring}}$ ) of maximum atomic density in  $|\downarrow\rangle$  as a function of  $m_z$ , together with the computed average momenta of the BIS. Dashed lines mark  $R_{\text{ring}} = 0$  and  $\sqrt{2}k_0$ , respectively. Error bars represent  $1\sigma$  statistical uncertainties.

$W = 0$ . These results reveal the 1D-2D crossover of SO couplings in our fermionic system, where the optimal 2D SO coupling is chosen as the experimental condition for subsequent measurements.

Next, we perform tomographic studies of the two lowest energy bands using PPQM at various two-photon detunings. We choose  $V_{0X\uparrow} = V_{0Y\uparrow} = 0.6E_0$ ,  $V_{0X\downarrow} = V_{0Y\downarrow} = 0.3E_0$ ,  $\Omega_{01} = 0.53E_0$  and  $\Omega_{02} = 0.22E_0$ , where  $E_0 = \frac{\hbar^2 k_0^2}{2m}$  is the recoil energy. Fig. 3(a) shows that under different  $m_z$  values, atoms are pumped to the  $|\downarrow\rangle$  state at different quasi-momenta in the first Brillouin zone (FBZ), and the maximum density of these  $|\downarrow\rangle$  atoms shows ring-like structures in the 2D distributions. As  $m_z$  increases from negative to positive, the ring structure shrinks towards the center of FBZ ( $\Gamma$  point), which characterizes a topological transition [26]. Fig. 3(b) shows numerical simulations that are very similar to the measurements. We further perform azimuthal averaging of each 2D distribution in Fig. 3(a) and then extract a “ring radius”  $R_{\text{ring}}$  that corresponds to the maximum density in the 1D profile, as showcased in Fig. 3(c) and (d). In Fig. 3(e), the measured ring radii  $R_{\text{ring}}$  are presented together with a series of computed average radii of the BISs [23], showing

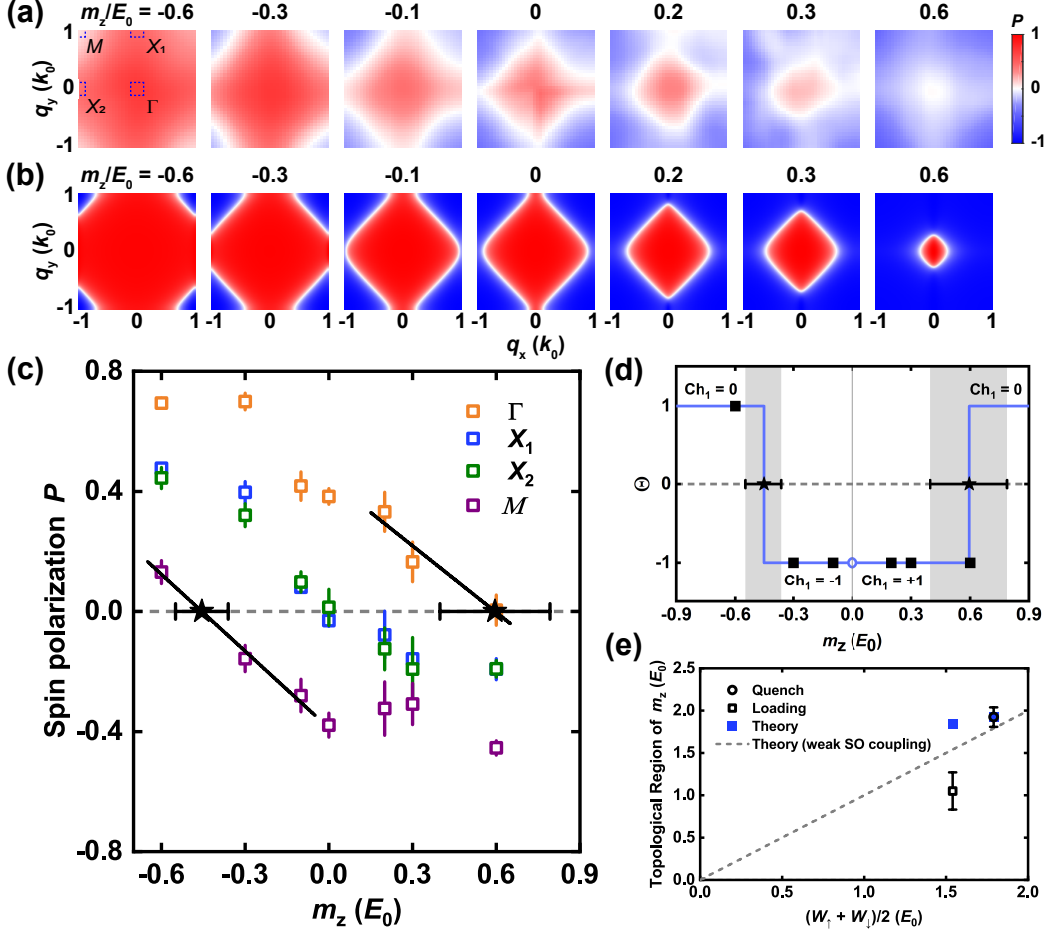


FIG. 4. Determination of band topology. (a) Measurement of spin textures after slowly loading the atoms into optical Raman lattices. The red and blue colors denote  $|\uparrow\rangle$  and  $|\downarrow\rangle$ , respectively. (b) Numerical simulations for zero temperature. (c) Spin polarizations at four highly symmetric momenta in the FBZ:  $\Gamma$  ( $0, 0$ ),  $X_1$  ( $0, \pm k_0$ ),  $X_2$  ( $\pm k_0, 0$ ), and  $M$  ( $\pm k_0, \pm k_0$ ). (d) The sign product  $\Theta = \prod_{i=1}^4 \text{sgn}[P(\Lambda_i)]$  and extracted Chern number  $Ch_1$  as a function of  $m_z$ . (e) Widths of the topological regime for  $m_z$ : PPQM (empty circles), loading measurement (empty squares), theory under experimental conditions (solid squares), and theory under vanishing SO couplings (dashed line). Here  $(W_↑ + W_↓)/2$  is the average of the bare ground bandwidths for  $|\uparrow\rangle$  and  $|\downarrow\rangle$ . Error bars represent  $1\sigma$  statistical uncertainties.

good agreement between the measured and computed values. In particular, our measurements cross with the upper and lower boundaries of  $R_{\text{ring}}$  at two  $m_z$  values separated by  $(9.3 \pm 0.6)$  kHz, corresponding to a width of  $(1.93 \pm 0.12)$   $E_0$ . This result agrees well with the predicted width of  $1.93 E_0$  for the topological regime, showing the remarkable feature that the PPQM protocol reveals accurate information of the topological band structures for the QAH model, which again demonstrates the generic effectiveness and robustness of our method.

*Determination of band topology.*— In order to further reveal the energy band topology, we measure the spin textures after a Fermi gas is slowly loaded into the optical Raman lattices. For this purpose, the Fermi gas is initially populated in the  $|\uparrow\rangle$  state and then slowly loaded into 2D optical Raman lattices in 11 ms and further held for 1 ms. Here, the two-photon detuning remains fixed during the loading process; we choose  $V_{0X\uparrow} = V_{0Y\uparrow} = 0.7E_0$ ,  $V_{0X\downarrow} = V_{0Y\downarrow} = 1.2E_0$ ,  $\Omega_{01} = 0.80E_0$  and  $\Omega_{02} = 0.33E_0$ . As shown in Fig. 4(a), the majority of atoms occupy the  $|\uparrow\rangle$  state at  $m_z = -0.6E_0$ , while they occupy the  $|\downarrow\rangle$  state at  $m_z = 0.6E_0$ . The spin texture experiences a smooth change between these two cases as  $m_z$  increases. Fig. 4(b) shows the corresponding simulations for zero temperature, exhibiting similar behaviors as the measurements [23]. Based on the spin textures, we determine the spin polarizations  $P(\Lambda_i)$  at four highly symmetric points  $\Lambda_{1,2,3,4} = \Gamma(0,0)$ ,  $X_1(0,\pm k_0)$ ,  $X_2(\pm k_0,0)$ , and  $M(\pm k_0,\pm k_0)$  in the FBZ (Fig. 4(c)), and further determine the Chern number according to the signs of  $P(\Lambda_i)$  [15, 23, 44]. As shown in Fig. 4(d), we extract a trivial-to-topological transition at  $m_z/E_0 = (-0.46 \pm 0.09)$ , and another topological-to-trivial phase boundary at  $m_z/E_0 = (0.60 \pm 0.20)$ . These experimentally determined phase boundaries are to be compared with a theoretical prediction of  $m_z/E_0 \approx \pm 0.93$ ; the measured topological regime has a width that is 57% of the prediction (Fig. 4(e)). By comparison, PPQM determines a width of topological regime that is  $(100 \pm 6)\%$  of the prediction. Therefore, both the loading measurement and PPQM reveal the band topologies and are consistent with each other. Furthermore, PPQM is superior in accurately determining the phase boundaries.

*Discussion and conclusion.*— We discuss the lifetime of our system. Near  $m_z = 0$ , we hold the SO-coupled fermions for different periods of time, measure the decay of the total atom number, and determine a  $1/e$  lifetime. We determine a lifetime  $\tau_0 \approx 16$  ms in typical experimental configurations for two-spin 2D-SO-coupled Fermi gases and  $\tau_1 \approx 117$  ms in a special configuration for a ten-spin 2D-SO-coupled gas [23]. At present,  $\tau_0$  is limited by technical impediments such as residual moving lattice potentials and has not reached the scattering-rate-limited value [23]. In future experiments, we expect to enhance the lifetime  $\tau_0$  to over 100 ms based on several improvements: implementing a new optical Raman lattice scheme that eliminates moving lattice potentials, further purifying the frequency mode of optical beams, and improving the homogeneity of optical traps. With a longer lifetime, the realization of a QAH system for SO-coupled ultracold fermions shall facilitate further studies of equilibrium and non-equilibrium topological physics.

In summary, we have realized the Qi-Wu-Zhang model with 2D-SO-coupled ultracold Fermi gases. We developed a novel and robust pump-probe quench measurement protocol to probe topological band structures, with the heating effect being minimized. The band topology with

2D SO coupling is observed by measuring the BISs and spin textures. The realization of the QAH model with spinful ultracold fermions enables the tuning of on-site interactions [45] and can provide a platform for further studies of the interplay between quantum correlations and topological physics [46, 47]. Future developments of our system also hold the promise to study correlated quantum dynamics [26, 48–50], simulate dynamical gauge fields [51–55], and explore topological superfluids [13, 56–58] and topological orders in the interacting regimes [59–61].

*Acknowledgments.*—We are grateful to Jing Zhang for insightful discussions. We acknowledge Shuai Chen, Cheng Chin, Biao Wu and Li You for discussions and technical support. This work is supported by the National Key Research and Development Program of China under Grant Nos 2018YFA0305601 and 2016YFA0300901, the National Natural Science Foundation of China (No. 11874073, 11825401, and 11761161003), and by the Open Project of Shenzhen Institute of Quantum Science and Engineering (Grant No. SIQSE202003). X.-J.L. and X.Z. conceived the project. M.-C.L., Y.-D.W., X.-J.W., H.Z., W.-W.W., and W.Q. performed the experiments. L.Z., M.-C.L., and Y.-D.W. performed the numerical computations. All authors contribute to the writing and revising of this manuscript.

---

[1] K. He, Y. Wang, and Q.-K. Xue, *National Science Review* **1**, 38 (2014).

[2] C.-X. Liu, S.-C. Zhang, and X.-L. Qi, *Annu. Rev. Condens. Matter Phys.* **7**, 301 (2016).

[3] F. D. M. Haldane, *Physical Review Letters* **61**, 2015 (1988).

[4] C.-Z. Chang, J. Zhang, X. Feng, J. Shen, Z. Zhang, M. Guo, K. Li, Y. Ou, P. Wei, L.-L. Wang, Z.-Q. Ji, Y. Feng, S. Ji, X. Chen, J. Jia, X. Dai, Z. Fang, S.-C. Zhang, K. He, Y. Wang, L. Lu, X.-C. Ma, and Q.-K. Xue, *Science* **340**, 167 (2013).

[5] J. G. Checkelsky, R. Yoshimi, A. Tsukazaki, K. S. Takahashi, Y. Kozuka, J. Falson, M. Kawasaki, and Y. Tokura, *Nature Physics* **10**, 731 (2014).

[6] X. Kou, S.-T. Guo, Y. Fan, L. Pan, M. Lang, Y. Jiang, Q. Shao, T. Nie, K. Murata, J. Tang, Y. Wang, L. He, T.-K. Lee, W.-L. Lee, and K. L. Wang, *Physical Review Letters* **113**, 137201 (2014).

[7] M. Z. Hasan and C. L. Kane, *Reviews of Modern Physics* **82**, 3045 (2010).

[8] X.-L. Qi and S.-C. Zhang, *Reviews of Modern Physics* **83**, 1057 (2011).

[9] K. He and Q.-K. Xue, *SPIN* **9**, 1940016 (2019).

[10] X.-L. Qi, Y.-S. Wu, and S.-C. Zhang, *Physical Review B* **74**, 085308 (2006).

[11] J. K. Asbóth, L. Oroszlány, and A. Pályi, *A Short Course on Topological Insulators* (Springer, 2016).

[12] G. Jotzu, M. Messer, R. Desbuquois, M. Lebrat, T. Uehlinger, D. Greif, and T. Esslinger, *Nature* **515**, 237 (2014).

[13] X.-J. Liu, K. T. Law, and T. K. Ng, *Physical Review Letters* **112**, 086401 (2014).

- [14] B.-Z. Wang, Y.-H. Lu, W. Sun, S. Chen, Y. Deng, and X.-J. Liu, *Physical Review A* **97**, 011605(R) (2018).
- [15] Z. Wu, L. Zhang, W. Sun, X.-T. Xu, B.-Z. Wang, S.-C. Ji, Y. Deng, S. Chen, X.-J. Liu, and J.-W. Pan, *Science* **354**, 83 (2016).
- [16] W. Sun, B.-Z. Wang, X.-T. Xu, C.-R. Yi, L. Zhang, Z. Wu, Y. Deng, X.-J. Liu, S. Chen, and J.-W. Pan, *Physical Review Letters* **121**, 150401 (2018).
- [17] W. Sun, C.-R. Yi, B.-Z. Wang, W.-W. Zhang, B. C. Sanders, X.-T. Xu, Z.-Y. Wang, J. Schmiedmayer, Y. Deng, X.-J. Liu, S. Chen, and J.-W. Pan, *Physical Review Letters* **121**, 250403 (2018).
- [18] A. J. Daley, *Quantum Inf Process* **10**, 865 (2011).
- [19] B. Song, C. He, S. Zhang, E. Hajiiev, W. Huang, X.-J. Liu, and G.-B. Jo, *Physical Review A* **94**, 061604(R) (2016).
- [20] S. Kolkowitz, S. L. Bromley, T. Bothwell, M. L. Wall, G. E. Marti, A. P. Koller, X. Zhang, A. M. Rey, and J. Ye, *Nature* **542**, 66 (2017).
- [21] G. W. F. Drake (Ed.), *Atomic, Molecular, & Optical Physics Handbook* (American Institute of Physics, Woodbury, N.Y., 1996).
- [22] J. Ye, H. J. Kimble, and H. Katori, *Science* **320**, 1734 (2008).
- [23] M.-C. Liang, Y.-D. Wei, L. Zhang, X.-J. Wang, H. Zhang, W.-W. Wang, W. Qi, X.-J. Liu, and X. Zhang, *Supplemental Material* (2021).
- [24] X.-T. Xu, Z.-Y. Wang, R.-H. Jiao, C.-R. Yi, W. Sun, and S. Chen, *Rev. Sci. Instrum.* **90**, 054708 (2019).
- [25] W. Qi, M.-C. Liang, H. Zhang, Y.-D. Wei, W.-W. Wang, X.-J. Wang, and X. Zhang, *Chin. Phys. lett.* **36**, 093701 (2019).
- [26] L. Zhang, L. Zhang, S. Niu, and X.-J. Liu, *Science Bulletin* **63**, 1385 (2018).
- [27] H. Hu and E. Zhao, *Physical Review Letters* **124**, 160402 (2020).
- [28] B. Zhu, Y. Ke, H. Zhong, and C. Lee, *Physical Review Research* **2**, 023043 (2020).
- [29] J. Ye and F. Li, *Physical Review A* **102**, 042209 (2020).
- [30] X.-L. Yu, W. Ji, L. Zhang, Y. Wang, J. Wu, and X.-J. Liu, *PRX Quantum* **2**, 020320 (2021).
- [31] L. Li, W. Zhu, and J. Gong, *Science Bulletin* **66**, 1502 (2021).
- [32] B. Song, C. He, S. Niu, L. Zhang, Z. Ren, X.-J. Liu, and G.-B. Jo, *Nature Physics* **15**, 911 (2019).
- [33] C.-R. Yi, L. Zhang, L. Zhang, R.-H. Jiao, X.-C. Cheng, Z.-Y. Wang, X.-T. Xu, W. Sun, X.-J. Liu, S. Chen, and J.-W. Pan, *Physical Review Letters* **123**, 190603 (2019).
- [34] Y. Wang, W. Ji, Z. Chai, Y. Guo, M. Wang, X. Ye, P. Yu, L. Zhang, X. Qin, P. Wang, F. Shi, X. Rong, D. Lu, X.-J. Liu, and J. Du, *Physical Review A* **100**, 052328 (2019).
- [35] B. Song, L. Zhang, C. He, T. F. J. Poon, E. Hajiiev, S. Zhang, X.-J. Liu, and G.-B. Jo, *Science Advances* **4**, eaao4748 (2018).
- [36] Z.-Y. Wang, X.-C. Cheng, B.-Z. Wang, J.-Y. Zhang, Y.-H. Lu, C.-R. Yi, S. Niu, Y. Deng, X.-J. Liu, S. Chen, and J.-W. Pan, *Science* **372**, 271 (2021).

[37] N. Flaschner, B. S. Rem, M. Tarnowski, D. Vogel, D.-S. Luhmann, K. Sengstock, and C. Weitenberg, *Science* **352**, 1091 (2016).

[38] M. Tarnowski, F. N. Unal, N. Flaschner, B. S. Rem, A. Eckardt, K. Sengstock, and C. Weitenberg, *Nature Communications* **10**, 1728 (2019).

[39] W. Ji, L. Zhang, M. Wang, L. Zhang, Y. Guo, Z. Chai, X. Rong, F. Shi, X.-J. Liu, Y. Wang, and J. Du, *Physical Review Letters* **125**, 020504 (2020).

[40] B. Chen, S. Li, X. Hou, F. Ge, F. Zhou, P. Qian, F. Mei, S. Jia, N. Xu, and H. Shen, *Photonics Research* **9**, 81 (2020).

[41] J. Niu, T. Yan, Y. Zhou, Z. Tao, X. Li, W. Liu, L. Zhang, H. Jia, S. Liu, Z. Yan, Y. Chen, and D. Yu, *Science Bulletin* **66**, 1168 (2021).

[42] P. Wang, Z.-Q. Yu, Z. Fu, J. Miao, L. Huang, S. Chai, H. Zhai, and J. Zhang, *Physical Review Letters* **109**, 095301 (2012).

[43] L. W. Cheuk, A. T. Sommer, Z. Hadzibabic, T. Yefsah, W. S. Bakr, and M. W. Zwierlein, *Physical Review Letters* **109**, 095302 (2012).

[44] X.-J. Liu, K. T. Law, T. K. Ng, and P. A. Lee, *Physical Review Letters* **111**, 120402 (2013).

[45] R. Zhang, Y. Cheng, P. Zhang, and H. Zhai, *Nature Reviews Physics* **2**, 213 (2020).

[46] M. Hohenadler and F. F. Assaad, *J. Phys.: Condens. Matter* **25**, 143201 (2013).

[47] S. Rachel, *Rep. Prog. Phys.* **81**, 116501 (2018).

[48] M. McGinley and N. R. Cooper, *Physical Review Research* **1**, 033204 (2019).

[49] L. Pastori, S. Barbarino, and J. C. Budich, *Physical Review Research* **2**, 033259 (2020).

[50] L. Zhang, L. Zhang, Y. Hu, S. Niu, and X.-J. Liu, *Physical Review B* **103**, 224308 (2021).

[51] J. Dalibard, F. Gerbier, G. Juzeliūnas, and P. Öhberg, *Reviews of Modern Physics* **83**, 1523 (2011).

[52] N. Goldman, G. Juzeliūnas, P. Öhberg, and I. B. Spielman, *Rep. Prog. Phys.* **77**, 126401 (2014).

[53] U.-J. Wiese, *Ann. Phys.* **525**, 777 (2013).

[54] E. Zohar, J. I. Cirac, and B. Reznik, *Rep. Prog. Phys.* **79**, 014401 (2016).

[55] M. Aidelsburger, L. Barbiero, A. Bermudez, T. Chanda, A. Dauphin, D. Gonzalez-Cuadra, P. R. Grzybowski, S. Hands, F. Jendrzejewski, J. Junemann, G. Juzeliūnas, V. Kasper, A. Piga, S.-J. Ran, M. Rizzi, G. Sierra, L. Tagliacozzo, E. Tirrito, T. V. Zache, J. Zakrzewski, E. Zohar, and M. Lewenstein, arXiv:2106.03063.

[56] X.-L. Qi, T. L. Hughes, and S.-C. Zhang, *Physical Review B* **82**, 184516 (2010).

[57] C. Zhang, S. Tewari, R. M. Lutchyn, and S. D. Sarma, *Physical Review Letters* **101**, 160401 (2008).

[58] M. Sato, Y. Takahashi, and S. Fujimoto, *Physical Review Letters* **103**, 020401 (2009).

[59] X.-J. Liu, Z.-X. Liu, K. T. Law, W. V. Liu, and T. K. Ng, *New Journal of Physics* **18**, 035004 (2016).

[60] J. Radic, A. D. Ciolo, K. Sun, and V. Galitski, *Physical Review Letters* **109**, 085303 (2012).

[61] W. S. Cole, S. Zhang, A. Paramekanti, and N. Trivedi, *Physical Review Letters* **109**, 085302 (2012).

[62] J. H. Denschlag, J. E. Simsarian, H. Haffner, C. McKenzie, A. Browaeys, D. Cho, K. Helmerson, S. L. Rolston, and W. D. Phillips, *J. Phys. B: At. Mol. Opt. Phys.* **35**, 3095 (2002).

## SUPPLEMENTAL MATERIAL

### I. PREPARATION AND DETECTION OF STRONTIUM FERMI GASES

#### A. Optical pumping and evaporative cooling

The realization of the Qi-Wu-Zhang model for quantum anomalous Hall phase relies on two-dimensional (2D) SO couplings. In our system, this model is realized via 2D SO couplings induced by 2D optical Raman lattices based on two-photon Raman transitions between a pair of spin states of fermionic strontium ( $^{87}\text{Sr}$ ) atoms:  $|\uparrow\rangle \equiv {}^1\text{S}_0 |F = \frac{9}{2}, m_F = \frac{9}{2}\rangle$  and  $|\downarrow\rangle \equiv |\frac{9}{2}, \frac{7}{2}\rangle$ . For  $^{87}\text{Sr}$ , the nuclear spin  $I$  equals  $\frac{9}{2}$  and the ground state  ${}^1\text{S}_0$  has ten magnetic sublevels. In our experiment, it is necessary to initially polarize the atoms to the  $|\uparrow\rangle$  state before loading them into optical Raman lattices.

To achieve a Fermi gas that is as spin-polarized as possible and still reach fairly low temperatures, we apply a circularly ( $\sigma^+$ -) polarized, frequency-modulated optical pumping laser that interrogates the  ${}^1\text{S}_0 |F = \frac{9}{2}\rangle \rightarrow {}^3\text{P}_0 |F' = \frac{9}{2}\rangle$  689-nm transitions before the evaporative cooling process. We note that in a 100%-spin-polarized Fermi gas, s-wave collisions are forbidden, and p-wave (or higher-order-wave) collisions under low-temperatures are strongly suppressed by energy barriers. Therefore, we carefully engineer the power, frequency modulation, and pulse length of the optical pumping beam as well as the magnetic field such that (1) during the evaporation, the atoms are partially polarized and can still experience effective collisions and (2) at the end of the evaporation, about 85% of the atoms occupy the state  $|\uparrow\rangle$  with a temperature of less than 200 nK.

#### B. Optical a.c. Stark shift

The optical a.c. Stark shift beam has a vertical polarization that is aligned with the direction of the magnetic field  $\mathbf{B}$ , which corresponds to a  $\pi$  polarization. Due to the narrow linewidth ( $\Gamma \approx 7.5$  kHz) of the  ${}^1\text{S}_0 \rightarrow {}^3\text{P}_1$  transition and the hyperfine splitting energy structure of the  ${}^3\text{P}_1$  manifold of strontium atoms, the a.c. Stark shift is non-linear with respect to the magnetic quantum number  $m_F$ . For example, when the differential a.c. Stark shift is 100 kHz between the  $|\uparrow\rangle$  and  $|\downarrow\rangle$  states, the same shift beam intensity will lead to a differential shift of only 75 kHz between the  $|\frac{9}{2}, \frac{7}{2}\rangle$  and  $|\frac{9}{2}, \frac{5}{2}\rangle$  states. Therefore, by properly choosing the frequency difference between the two Raman beams, we can realize near-resonance two-photon Raman transitions only between the  $|\uparrow\rangle$  and  $|\downarrow\rangle$  states; that is to say, the a.c. Stark shift beam isolates the  $|\uparrow\rangle$  and  $|\downarrow\rangle$  states from the

rest of the spin ground states.

### C. Spin-resolved time-of-flight measurements

In order to extract the momentum distributions of the  $|\uparrow\rangle$  and  $|\downarrow\rangle$  states, we perform a spin-resolved time-of-flight (TOF) detection that comprises of three measurements under different conditions. In the first measurement, shortly after the traps are shut off and TOF starts, we pulse on a  $\sigma^+$ -polarized, frequency-modulated ‘Blast’ beam [19] that removes the  $|\uparrow\rangle$  state by interrogating the  $|F = \frac{9}{2}, m_F = \frac{9}{2}\rangle \rightarrow |F' = \frac{11}{2}, m_F = \frac{11}{2}\rangle$  transition, which is followed by additional TOF expansion and a final 461-nm absorption imaging, producing a momentum distribution  $I_1$ . Similarly, in the second measurement, we change the frequency modulation range of the Blast beam to remove both the  $|\uparrow\rangle$  and  $|\downarrow\rangle$  states, producing a momentum distribution  $I_2$ . In the third measurement, we apply no Blast pulse and measure the momentum distribution  $I_0$  of all spin states. Based on these three measurements, the momentum distributions of the  $|\uparrow\rangle$  and  $|\downarrow\rangle$  states are extracted as  $I_0 - I_1$  and  $I_1 - I_2$ , respectively.

In Fig. 2 of the main text, we directly analyze the time-of-flight images, which show the mechanical momentum distributions. In Figs. 3 and 4, we map the TOF results to the quasi-momentum space of the optical Raman lattice with a procedure similar to that employed in the works on 2D-SO-coupled ultracold bosons [15, 17].

## II. COHERENCE BETWEEN TWO RAMAN COUPLINGS UNDER A 1D SO COUPLING CONFIGURATION

The realization of a 2D SO coupling depends on the coherent superposition of two lattices of Raman couplings. Before realizing a 2D SO coupling, we first use a 1D SO-coupled Fermi gas to verify the coherence between two sets of Raman couplings in the double- $\Lambda$  configuration (see Fig. 1(b) in the main text). In this simplified case, we can directly measure the Raman Rabi oscillation and show the variation of a total Rabi frequency as a function of a controlled relative phase between two sets of Raman couplings.

In a setup similar to that in Fig. 1(a) of the main text but without the retro-reflecting mirrors, two linearly polarized ‘‘Raman’’ beams cross at the atoms, with their polarizations each rotated by  $58^\circ$  from the vertical direction. A variable composite wave plate  $\lambda_{\text{ph}}$  (with retardation  $\varphi_{\text{ctrl}}$ ) is placed in the Raman beam along the  $-\hat{Y}$  direction to tune the relative phase between  $E_{YZ}$  and

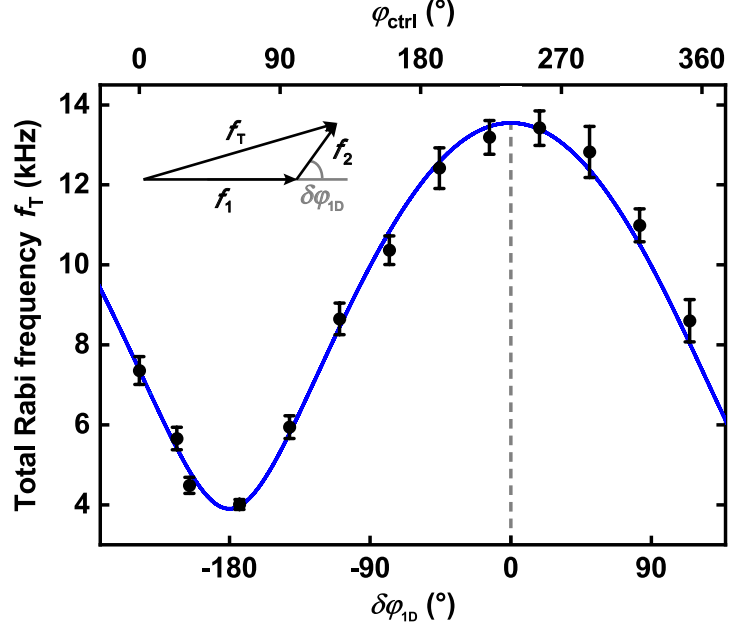


FIG. S1. Coherent interference between two 1D SO Raman couplings in the double- $\Lambda$  configuration. The total Rabi frequency  $f_T$  varies when the relative phase  $\delta\varphi_{1D}$  between two Raman couplings changes. The black dots are the measurements, and the blue line is a fit to a three-parameter function  $f_T = \sqrt{f_1^2 + f_2^2 + 2f_1f_2 \cos(\varphi_{ctrl} + \delta\varphi_{1D,offset})}$  where the parameters are determined as  $f_1 = 8.7$  kHz,  $f_2 = 4.8$  kHz, and  $\delta\varphi_{1D,offset} \equiv (\delta\varphi_{1D} - \varphi_{ctrl}) \bmod 360^\circ = 122.4^\circ$ .

$E_{YX}$ . In this way, the relative phase  $\delta\varphi_{1D}$  between the two Raman couplings can be controlled. As illustrated by the inset of Fig. S1, the total Rabi frequency  $f_T$  is obtained by the superposition of two individual Raman couplings  $f_1$  and  $f_2$ , which depends on  $\delta\varphi_{1D}$ . This total Rabi frequency can be determined via Raman Rabi oscillation measurements. As shown in Fig. S1, the measured  $f_T$  varies with  $\varphi_{ctrl}$  and can be well described by a model with a phase period of  $360^\circ$ . The finite offset  $\delta\varphi_{1D,offset}$  is potentially due to the difference between phase retardations of s- and p-polarizations when each Raman beam passes through optical components such as lenses, mirrors, and vacuum chamber viewports. Take this phase offset into account, we define  $\delta\varphi_{1D} = 0$  as the phase difference where the total Rabi frequency  $f_T$  reaches its maximum, and can then rewrite this total Rabi frequency as  $f_T = \sqrt{f_1^2 + f_2^2 + 2f_1f_2 \cos(\delta\varphi_{1D})}$ . This function describes the measured  $f_T$  very well and the fitted  $f_1$  and  $f_2$  agree with the predicted values based on the Raman beam powers and waists. These results thus demonstrate the coherence between two Raman couplings, which lays the foundation of 2D SO couplings.

### III. 1D-2D CROSSOVER OF SO COUPLINGS

Loading ultracold fermions into 2D optical Raman lattices realizes a minimal model of quantum anomalous Hall (QAH) Hamiltonian, namely the Qi-Wu-Zhang model:

$$\hat{H} = \frac{\mathbf{p}^2}{2m} + V_{\text{latt}}(x, y) + \Omega_R(x, y) + \frac{\delta_0}{2}\sigma_z. \quad (\text{S1})$$

Here, the Raman coupling matrix is given by

$$\Omega_R(x, y) = \begin{pmatrix} 0 & \Omega_1 + e^{i\delta\varphi}\Omega_2 \\ \Omega_1^* + e^{-i\delta\varphi}\Omega_2^* & 0 \end{pmatrix}, \quad (\text{S2})$$

where  $\Omega_1(x, y) = \Omega_{01} \sin k_0 x \cos k_0 y$ ,  $\Omega_2(x, y) = \Omega_{02} \cos k_0 x \sin k_0 y$ , and  $\delta\varphi$  is the relative phase between two sets of Raman couplings. In order to better understand the 1D-2D crossover of the SO coupling when  $\delta\varphi$  varies, we rewrite Eq. S2 as follows:

$$\Omega_R(x, y) = \sigma_x(\Omega_1 + \Omega_2 \cos \delta\varphi) - \sigma_y \Omega_2 \sin \delta\varphi, \quad (\text{S3})$$

where  $\sigma_x$  and  $\sigma_y$  are Pauli matrices. At  $\delta\varphi = \pm 90^\circ$ ,  $\Omega_R(x, y) = \sigma_x \Omega_1 \mp \sigma_y \Omega_2$  represents the optimal 2D SO coupling configurations. At  $\delta\varphi = 0^\circ$  or  $180^\circ$ ,  $\Omega_R(x, y) = \sigma_x(\Omega_1 \pm \Omega_2)$  represents a configuration that most closely resembles a 1D SO coupling for fermions [19, 42, 43]. In particular, if  $\Omega_{01} = \Omega_{02}$  and  $\delta\varphi = 0^\circ$  or  $180^\circ$ ,  $\Omega_R$  will reach a purely 1D SO configuration in a way that is demonstrated for ultracold bosons [16].

#### A. Relative phase control with a variable composite waveplate

To tune  $\delta\varphi$  and show the 1D-2D crossover of SO couplings, we implement a variable composite waveplate  $\lambda_{\text{ph}}$  using three waveplates. Under the basis of vertical and horizontal (V and H) polarizations, the unitary transformation matrix of a half-waveplate (HW) or a quarter-waveplate (QW) acting on a transmitting laser beam is given by

$$U_{\text{HW}}(\theta) = \begin{pmatrix} \cos^2 \theta - \sin^2 \theta & 2 \cos \theta \sin \theta \\ 2 \cos \theta \sin \theta & \sin^2 \theta - \cos^2 \theta \end{pmatrix},$$

$$U_{\text{QW}}(\theta) = \begin{pmatrix} \cos^2 \theta + i \sin^2 \theta & (1 - i) \cos \theta \sin \theta \\ (1 - i) \cos \theta \sin \theta & \sin^2 \theta + i \cos^2 \theta \end{pmatrix}, \quad (\text{S4})$$

where the beam propagates along a horizontal direction,  $\theta$  represents the angle between the slow axis of a waveplate and the vertical direction, and the vertical and horizontal polarizations corresponds to  $\begin{pmatrix} 1 \\ 0 \end{pmatrix}$  and  $\begin{pmatrix} 0 \\ 1 \end{pmatrix}$ , respectively.

In our three-waveplate configuration, a half-waveplate is sandwiched between two quarter-waveplates. The slow axes of both quarter-waveplates are fixed to the same angle ( $45^\circ$  with respect to the vertical direction), whereas the slow axis of the half-waveplate has a tunable angle  $\varphi_{\text{HW}}$ . Thus the total transformation matrix of this variable composite waveplate  $\lambda_{\text{ph}}$  is given below:

$$U_{\text{QW}}(45^\circ)U_{\text{HW}}(\varphi_{\text{HW}})U_{\text{QW}}(45^\circ) = ie^{-i \cdot 2\varphi_{\text{HW}}} \begin{pmatrix} 1 & 0 \\ 0 & -e^{i \cdot 4\varphi_{\text{HW}}} \end{pmatrix}. \quad (\text{S5})$$

Therefore, by choosing  $\varphi_{\text{HW}}$  for the half-waveplate, we implement an additional relative phase of  $4\varphi_{\text{HW}}$  between the horizontal and vertical polarizations, which in turn tunes the relative phase  $\delta\varphi$  between the two Raman couplings [16] by the same amount ( $4\varphi_{\text{HW}}$ ).

## B. Analysis of the measurements for 1D-2D crossover

In our quench measurements for the 1D-2D crossover (Fig. 2 in the main text), atoms are transferred from the  $|\uparrow\rangle$  state to the  $|\downarrow\rangle$  state by SO couplings. The Raman coupling term, Eq. S3, can be rewritten as

$$\begin{aligned} \Omega_R(x, y) = & \frac{1}{4i} [\sigma_x(\Omega_{01} + \Omega_{02} \cos \delta\varphi) - \sigma_y \Omega_{02} \sin \delta\varphi] [e^{ik_0(x+y)} - e^{-ik_0(x+y)}] \\ & + \frac{1}{4i} [\sigma_x(\Omega_{01} - \Omega_{02} \cos \delta\varphi) + \sigma_y \Omega_{02} \sin \delta\varphi] [e^{ik_0(x-y)} - e^{-ik_0(x-y)}]. \end{aligned} \quad (\text{S6})$$

Eq. S6 shows that the Raman coupling transfers momentum according to the exponential functions while it flips the spin state, which leads to the typical line segments displayed in Fig. 2(b) along the  $\hat{X} + \hat{Y}$  and  $\hat{X} - \hat{Y}$  directions.

In the limit of short pulses (when the pulse is short compared to the  $\pi$  pulse length for a Raman Rabi frequency of  $\Omega_{01} + \Omega_{02}$ ), the  $|\downarrow\rangle$  atom numbers for momentum transfer along the  $\hat{X} \pm \hat{Y}$  directions (namely  $N_{1+2} = N_1 + N_2$  and  $N_{3+4} = N_3 + N_4$  in the main text) are proportional to  $(\Omega_{01} \pm \Omega_{02} \cos \delta\varphi)^2 + (\Omega_{02} \sin \delta\varphi)^2$ , respectively. Thus the population imbalance is determined as follows:

$$\begin{aligned} W &= \frac{(N_1 + N_2) - (N_3 + N_4)}{(N_1 + N_2) + (N_3 + N_4)} \\ &= \frac{2(\Omega_{01}/\Omega_{02})}{(\Omega_{01}/\Omega_{02})^2 + 1} \cos \delta\varphi. \end{aligned} \quad (\text{S7})$$

Eq. S7 shows that the imbalance parameter  $W$  oscillates with the relative phase  $\delta\varphi$  in a form of  $W = W_{\text{max}} \cos \delta\varphi$ , where  $W_{\text{max}}$  is predicted to be  $\frac{2(\Omega_{01}/\Omega_{02})}{(\Omega_{01}/\Omega_{02})^2 + 1}$  in the short-pulse limit.

In our experimental configuration,  $\Omega_{01}/\Omega_{02} \approx 2.4$ , which leads to a predicted  $W_{\max,\text{theo}} \approx 0.71$  in the short-pulse limit. We further perform numerical simulations at the actual pulse length and observe that the variation of  $W$  with respect to  $\delta\varphi$  is still close to a cosine function. The simulation yields an oscillation amplitude  $W_{\max,\text{simu}} \approx 0.69$  for a  $200 \mu\text{s}$  pulse length in our experiment. From the fitted result of experimental data (Fig. 2(c) in the main text), we extract an oscillation amplitude  $W_{\max,\text{exp}} = 0.40 \pm 0.02$ , which is smaller than the predicted value. The difference between  $W_{\max,\text{exp}}$  and  $W_{\max,\text{theo}}$  or  $W_{\max,\text{simu}}$  may be caused by the finite temperature of our Fermi gases.

#### IV. PUMP-PROBE QUENCH MEASUREMENT (PPQM) AND NUMERICAL SIMULATION

##### A. A physical picture for PPQM

In this part, we provide a simple physical picture for our novel protocol of pump-probe quench measurement (PPQM). We denote the initial state as  $|\Psi(\mathbf{q})\rangle = \phi(\mathbf{q})|\uparrow\rangle$ , where  $|\phi(\mathbf{q})|^2$  describes the atomic density at quasi-momentum  $\mathbf{q}$ . When the Raman lattice is pulsed on, the evolution of the quantum state is described by the evolution operator  $\hat{U}(t) = \exp[-i\hat{\mathcal{H}}_f(\mathbf{q})t]$ , where  $\hat{\mathcal{H}}_f(\mathbf{q})$  is the post-quench Bloch Hamiltonian. Thus, the time-evolved spin polarization is determined by  $\langle\sigma_z(\mathbf{q},t)\rangle = \langle\uparrow|\hat{U}^\dagger(t)\sigma_z\hat{U}(t)|\uparrow\rangle$ . In other words, the spin-flip evolution is the same no matter whether atoms are prepared in an optical lattice or not. Furthermore, we measure the band-inversion surface (BIS) based on the transfer of atoms from the  $|\uparrow\rangle$  state to the  $|\downarrow\rangle$  state, which is insensitive to the atomic distribution  $|\phi(\mathbf{q})|^2$ . Therefore, our new protocol of PPQM not only effectively probes the BISs as has been achieved in the previous experiments [17], but also demonstrates a simplified method without the need of optical lattices before the quench, which suppresses heating and other detrimental effects.

We note that the analysis of the PPQM measurements can be further simplified under our experimental conditions. Because we use relatively shallow lattice depths for the post-quench Hamiltonian, the ground-band atoms appear mostly in the first Brillouin zone (FBZ) after the time-of-flight. Since this work focuses primarily on the  $|\uparrow\rangle \rightarrow |\downarrow\rangle$  spin flipping process between the SO-coupled ground bands, the majority of the corresponding atomic signal resides within the FBZ. We thus ignore the atomic signal outside the FBZ in the analysis of our PPQM measurements.

### B. Note on the experimentally chosen pulse duration

In the main text, we describe the advantages of PPQM, where “we only need a short pulse that generates the optical Raman lattice to pump the initial state to the other spin state” with a pulse duration  $T_{\text{quench}} = 200 \mu\text{s}$ . This pulse duration is chosen with the following considerations.

Firstly,  $T_{\text{quench}}$  cannot be too small. Otherwise, the signal of atoms transferred to  $|\downarrow\rangle$  at the BIS will also be small and proportional to  $(\Omega_{\text{mod}} T_{\text{quench}})^2$ , where  $\Omega_{\text{mod}}$  is the modified Rabi frequency. This small signal from the BIS can be overwhelmed by the “noise” contributed by the small amount of atoms transferred to  $|\downarrow\rangle$  at other quasi-momenta where the modified Rabi frequency is higher due to the larger two-photon detuning.

Secondly, instead of studying dynamical oscillations between two spin states, we only need to pump sufficient atoms from the  $|\uparrow\rangle$  state to the  $|\downarrow\rangle$  state. Therefore,  $T_{\text{quench}}$  does not need to be too large compared with the typical two-photon Raman Rabi oscillation period. In fact, it only needs to reach a fraction of the duration of a  $\pi$ -pulse for the minimum energy gap that is reached at the BIS.

In the main text, we describe the following Raman coupling parameters used in the PPQM:  $\Omega_{01} = 0.53E_0$  and  $\Omega_{02} = 0.22E_0$ , where  $E_0 \approx h \times 4.8 \text{ kHz}$  is the recoil energy at  $\lambda_0 \approx 689.4 \text{ nm}$ , and  $h$  is the Planck constant. Under an optimal 2D SO configuration, these parameters lead to a minimum energy gap (at the BIS) of  $\Delta_{\text{min}} \sim \sqrt{\Omega_{01}^2 + \Omega_{02}^2}/2 \approx 0.29E_0$  that also equals the characteristic Raman Rabi frequency. The corresponding  $\pi$ -pulse duration can then be determined as  $T_\pi = \frac{h}{2\Delta_{\text{min}}} \approx 360 \mu\text{s}$ . The experimentally chosen  $T_{\text{quench}}$  should not exceed  $T_\pi$ .

In the actual measurements, we have chosen  $T_{\text{quench}} = 200 \mu\text{s} \approx 0.56T_\pi$ , which satisfies the aforementioned two considerations.

### C. Numerical simulation of the band-inversion surfaces

We demonstrate the effectiveness and robustness of our PPQM protocol by numerically computing the BISs based on the equilibrium spin textures. For this purpose, we employ the plane-wave basis

$$\begin{aligned} |m, n\rangle_{\uparrow} &= C_{mn,\uparrow} |q_x + 2mk_0, q_y + 2nk_0\rangle, \\ |l, j\rangle_{\downarrow} &= C_{lj,\downarrow} |q_x + 2lk_0 + k_0, q_y + 2jk_0 + k_0\rangle, \end{aligned} \quad (\text{S8})$$

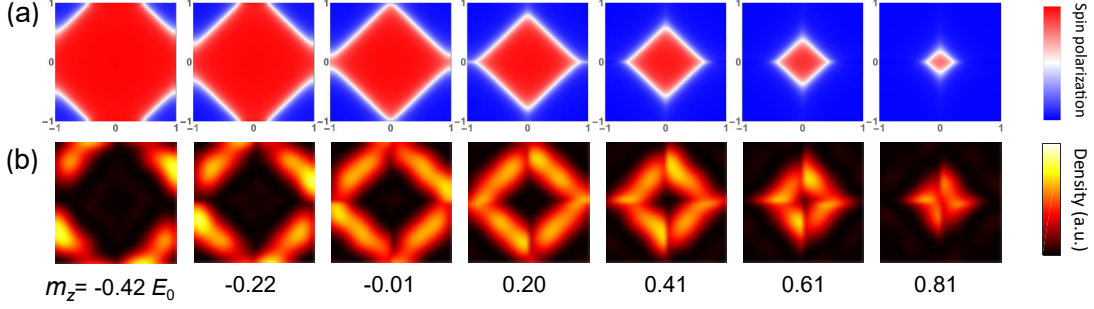


FIG. S2. Equilibrium spin textures and post-PPQM atomic distributions in the FBZ. (a) The computed equilibrium spin textures under the same parameters as those in the post-quench Hamiltonian for Fig. 3 in the main text. (b) Simulated distribution of  $|\downarrow\rangle$  atoms in the FBZ after the PPQM. The horizontal and vertical axes correspond to the  $q_x$  and  $q_y$  directions, respectively.

where and  $C_{mn,\uparrow}$  and  $C_{lj,\downarrow}$  are coefficients for normalization. The post-quench Bloch Hamiltonian during the Raman pulse is then expressed as

$$\begin{aligned} \hat{\mathcal{H}}_f = & \sum_{m,n,\sigma=\uparrow,\downarrow} V_\sigma (|m,n\rangle_\sigma \langle m,n+1|_\sigma + |m,n\rangle_\sigma \langle m+1,n|_\sigma) \\ & + \sum_{m',n'} \left[ (M_x + iM_y) |m',n'\rangle_\uparrow \langle m',n'|_\downarrow + \frac{\delta_0}{2} |m',n'\rangle_\uparrow \langle m',n'|_\uparrow - \frac{\delta_0}{2} |m',n'\rangle_\downarrow \langle m',n'|_\downarrow \right] \\ & + \text{h.c.} \end{aligned} \quad (\text{S9})$$

where  $M_{x/y}$  denotes the Raman couplings in the  $x/y$  direction, and  $\delta_0$  is the two-photon detuning. After diagonalizing  $\hat{\mathcal{H}}_f$ , the BISs are identified as momenta where the  $|\uparrow\rangle$  and  $|\downarrow\rangle$  populations are equal, and are denoted by white lines in Fig. S2(a) where the condition for simulations is the same as that in the post-quench Hamiltonian for Fig. 3 in the main text.

For comparison, the simulated 2D quasi-momentum distributions of the  $|\downarrow\rangle$  atoms following our PPQM protocol (Fig. 3(b) in the main text) are also shown here in Fig. S2(b), which agrees well with the computed BISs. These results further support the measurement-simulation agreement shown in Fig. 3(e) in the main text.

## V. DETERMINE THE BAND TOPOLOGY

The QAH Hamiltonian  $\hat{H}$  (given by Eq. 1 in the main text) satisfies an inversion symmetry defined by  $\hat{P} \equiv \hat{R}_{2D} \otimes \hat{\sigma}_z$  [15, 44]. Here,  $\hat{R}_{2D}$  represents a 2D spatial operator that transforms the Bravais lattice vector from  $\mathbf{R}$  to  $-\mathbf{R}$ , and  $\hat{\sigma}_z$  is the Pauli matrix. The Hamiltonian  $\hat{H}$  can be transformed to a form expressed in the momentum space, where we obtain the Bloch Hamiltonian

$\mathcal{H}(\mathbf{q})$  for a given quasi-momentum  $\mathbf{q}$ . It can be verified that  $\hat{P}\hat{H}\hat{P}^{-1} = \hat{H}$  and that the Bloch Hamiltonian satisfies  $\hat{P}\hat{\mathcal{H}}(\mathbf{q})\hat{P}^{-1} = \hat{\mathcal{H}}(-\mathbf{q})$  [44]. Thus at the four highly symmetric momenta  $\{\Lambda_i\} = \{\Gamma(0,0), X_1(0,k_0), X_2(k_0,0), M(k_0,k_0)\}$  in the FBZ, we have the commutation relation  $[\hat{\mathcal{H}}(\Lambda_i), \hat{P}] = 0$ . Therefore, the Bloch states are eigenstates of  $\hat{P}$  at the four highly symmetric momenta  $\Lambda_i$  with eigenvalues  $P(\Lambda_i)$ , and the signs of these four eigenvalues can be used to define a topological invariant that determines the band topology [15, 44]. Here, the first Chern number is given by

$$\text{Ch}_1 = -\frac{1-\Theta}{4} \sum_{i=1}^4 \text{sgn}[P(\Lambda_i)], \quad (\text{S10})$$

where the topological invariant  $\Theta$  is defined by

$$\Theta = \prod_{i=1}^4 \text{sgn}[P(\Lambda_i)]. \quad (\text{S11})$$

In the experiment, the measurement of spin-polarization at low but finite temperature can be applied to determine the Chern number of Bloch bands [15, 44].

## VI. LIFETIME MEASUREMENTS AND FUTURE IMPROVEMENTS

### A. Heating rate due to optical scattering

We estimate a heating rate by considering the single-photon scattering process. Such heating of Fermi gases in our system is mainly caused by the a.c. Stark shift beam and the optical Raman lattice beams. Here, the scattering rate is determined as

$$R_{\text{scatt}} = \frac{\Gamma}{2} \sum_{F'} \frac{2\Omega_{F'}^2/\Gamma^2}{1 + 2\Omega_{F'}^2/\Gamma^2 + 4\Delta_{F'}^2/\Gamma^2}, \quad (\text{S12})$$

where  $\Gamma = 7.5$  kHz is the natural linewidth of the  ${}^1\text{S}_0 \rightarrow {}^3\text{P}_1$  transition at 689 nm,  $\Delta_{F'}$  and  $\Omega_{F'}$  are the frequency detuning and Rabi frequency for a single-photon transition to a manifold of excited states with  $F' = 11/2, 9/2$  and  $7/2$ . The corresponding heating rate is then determined by the scattering rate  $R_{\text{scatt}}$  and the recoil energy  $E_0$ :

$$\dot{T} = \frac{E_0 R_{\text{scatt}}}{k_{\text{B}}}, \quad (\text{S13})$$

where  $k_{\text{B}}$  is the Boltzmann constant.

In our experiment with a relatively strong a.c. Stark shift beam (where the differential shift between  $|\uparrow\rangle$  and  $|\downarrow\rangle$  is about 100 kHz), the heating rate due to the aforementioned single-photon

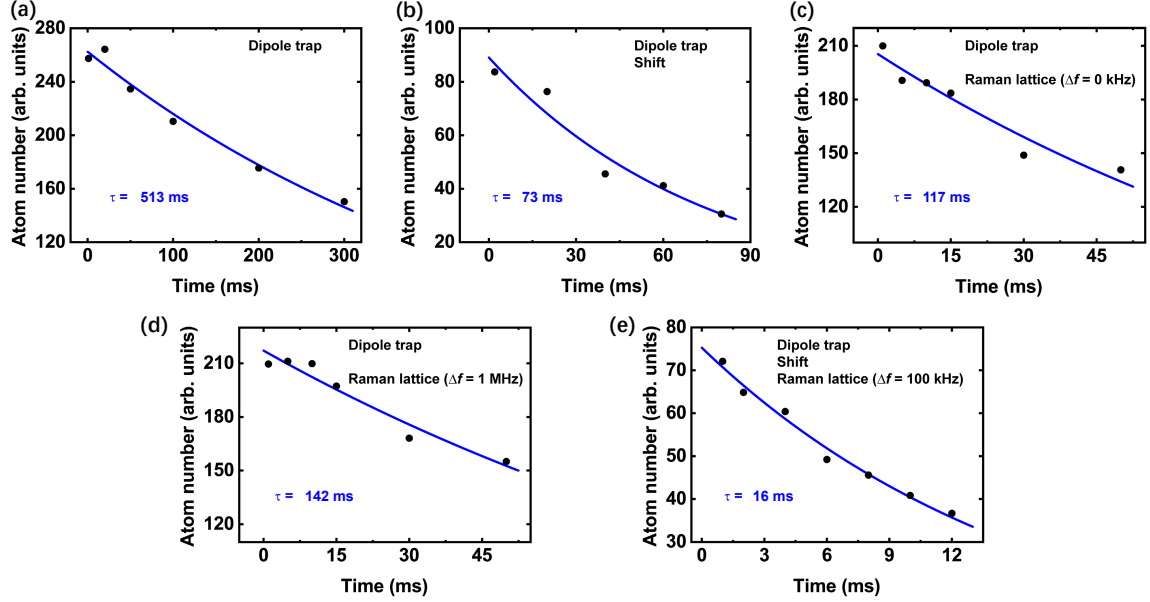


FIG. S3. Lifetime measurements under various experimental conditions. Black dots are the experimental data, and the blue lines are exponential fits. From these measured lifetime  $\tau$ , we can extract the contributions of various factors to the lifetime of the Fermi gas. Here,  $\Delta f$  is the frequency difference between two Raman lattice beams. (a) (Measurement with) dipole trap only. (b) Dipole trap and the a.c. Stark shift beam (where the differential shift between  $|\uparrow\rangle$  and  $|\downarrow\rangle$  is about 100 kHz). (c) Dipole trap and the optical Raman lattice beams with  $\Delta f = 0$  kHz (where the two-photon detuning is near zero without the a.c. Stark shift beam). (d) Dipole trap and the optical Raman lattice beams with  $\Delta f = 1$  MHz (where the two-photon detuning is large). (e) Dipole trap, the a.c. Stark shift beam, and the optical Raman lattice beams with  $\Delta f = 100$  kHz (where the two-photon detuning is near zero).

scattering ( $R_{\text{scatt}} \sim 14 \text{ s}^{-1}$ ) by the a.c. Stark shift beam is about 3 nK/ms, and the heating rate due to the optical Raman lattice beams is much smaller by more than a factor of ten. Thus the scattering limited lifetime of the Fermi gas is on the order of 100 ms.

## B. Lifetime measurements

We determine the lifetime of the Fermi gas by holding the atoms under a certain experimental condition and measuring the atom number as a function of the hold time. We use an exponential function to fit the decay of the total atom number. As shown in Fig. S3(e), the Fermi gas held in the optical Raman lattices with  $m_z \approx 0$  has a  $1/e$  lifetime of  $\tau_0 \approx 16$  ms, which is significantly shorter than the single-photon-scattering-limited value that is on the order of 100 ms. To investigate the reasons why the measured lifetime is much shorter than the scattering-limited value (estimated

in the previous subsection), we build a model to incorporate various possible heating sources as follows:

$$\frac{1}{\tau} = \frac{1}{\tau_{\text{dipole}}} + \frac{1}{\tau_{\text{shift}}} + \frac{1}{\tau_{\text{Raman}}} + \frac{1}{\tau_{\text{SOC}}} + \frac{1}{\tau_{\text{other}}}, \quad (\text{S14})$$

Here, the heating effects from the Raman lattice beams are divided into two parts:  $\tau_{\text{Raman}}$  denoting the contribution from single-photon scattering processes and  $\tau_{\text{SOC}}$  denoting the contribution from 2D SO couplings.

To evaluate each term in Eq. S14, we measure the atomic lifetime under various experimental conditions as shown in Fig. S3. From the measurements in Figs. S3(a) to (d), we can extract  $\tau_{\text{dipole}} \sim 513$  ms,  $\tau_{\text{shift}} \sim 85$  ms,  $\tau_{\text{Raman}} \sim 196$  ms, and  $\tau_{\text{SOC}} \sim 664$  ms. Then, based on the measurement in Fig. S3(e), the last term can be determined as  $\tau_{\text{other}} \sim 24$  ms, which is by far the most severe limitation on the atomic lifetime.

A highly likely cause of  $\tau_{\text{other}}$  is the heating due to moving optical lattices [62], which has a technical nature. Due to the limited power of the a.c. Stark shift beam (about 45 mW), The  $|\uparrow\rangle$  and  $|\downarrow\rangle$  states are separated by about 100 kHz, which dictates the frequency difference between two Raman beams to be around the same value for generating on-resonance SO couplings. In our current optical design, such frequency difference between the two Raman beams (as well as their retro-reflected beams) leads to time-varying and spatially periodic a.c. Stark shift potentials, namely moving optical lattices. Such moving lattices can drag the atoms and cause severe heating effects in the Fermi gas, which limits the atomic lifetime.

In order to sufficiently reduce the heating effects caused by move lattices and enhance the atomic lifetime, we design a new optical setup based on a novel double- $\Lambda$  Raman coupling scheme, where the characteristic frequency difference underlying the moving lattices are pushed to a few MHz, which is much further away from the typical frequency scales for physical processes in our optical Raman lattice experiment. Thus the expected heating rate can be significantly reduced, and the lifetime can be enhanced accordingly. After the completion of this work, we performed a preliminary test of the simplest version of our new setup, and observe that, encouragingly, the atomic lifetime has already been enhanced by a factor of 2. A full implementation of the new optical Raman lattice design holds promise for further enhancing the atomic lifetime towards the order of 100 ms. The corresponding research is well worth further investigations, which is beyond the scope of this paper and will be presented elsewhere.